

Research Paper

Photodynamic Therapy Induced Enhancement of Tumor Vasculature Permeability Using an Upconversion Nanoconstruct for Improved Intratumoral Nanoparticle Delivery in Deep Tissues

Weidong Gao, Zhaohui Wang, Liwei Lv, Deyan Yin, Dan Chen, Zhihao Han, Yi Ma, Min Zhang, Man Yang, Yueqing Gu 

State Key Laboratory of Natural Medicines, Department of Biomedical Engineering, School of Engineering, China Pharmaceutical University, Nanjing, 210009, P. R. China.

 Corresponding author: Yueqing Gu, Ph.D. Professor of State Key Laboratory of Natural Medicines, Department of Biomedical Engineering, School of Engineering, China Pharmaceutical University, Nanjing, 210009, P. R. China; e-mail: guyueqing@cpu.edu.cn phone: 86-25-83271046 fax: 86-25-83271249.

© Ivyspring International Publisher. Reproduction is permitted for personal, noncommercial use, provided that the article is in whole, unmodified, and properly cited. See <http://ivyspring.com/terms> for terms and conditions.

Received: 2016.02.13; Accepted: 2016.04.25; Published: 2016.05.21

Abstract

Photodynamic therapy (PDT) has recently emerged as an approach to enhance intratumoral accumulation of nanoparticles. However, conventional PDT is greatly limited by the inability of the excitation light to sufficiently penetrate tissue, rendering PDT ineffective in the relatively deep tumors. To address this limitation, we developed a novel PDT platform and reported for the first time the effect of deep-tissue PDT on nanoparticle uptake in tumors. This platform employed c(RGDyK)-conjugated upconversion nanoparticles (UCNPs), which facilitate active targeting of the nanoconstruct to tumor vasculature and achieve the deep-tissue photosensitizer activation by NIR light irradiation. Results indicated that our PDT system efficiently enhanced intratumoral uptake of different nanoparticles in a deep-seated tumor model. The optimal light dose for deep-tissue PDT (34 mW/cm^2) was determined and the most robust permeability enhancement was achieved by administering the nanoparticles within 15 minutes following PDT treatment. Further, a two-step treatment strategy was developed and validated featuring the capability of improving the therapeutic efficacy of Doxil while simultaneously reducing its cardiotoxicity. This two-step treatment resulted in a tumor inhibition rate of 79% compared with 56% after Doxil treatment alone. These findings provide evidence in support of the clinical application of deep-tissue PDT for enhanced nano-drug delivery.

Key words: Photodynamic therapy; Upconversion; EPR; Nanoparticles; Drug delivery.

Introduction

Nano-carriers have emerged as a novel platform for the delivery of diverse therapeutic agents, including chemotherapeutics, peptides, and small interfering RNAs [1,2]. It is reported that more than 240 nanomedicine products have been approved or under different stages of clinical trials [3]. For instance, Doxil and Genexol PM have been widely used in the clinical cancer treatment [4, 5]. Most of the nanodrugs in clinical trials take advantage of their

passive intratumoral accumulation after intravenous administration. This accumulation is due to the enhanced permeability and retention (EPR) effect. Since first discovered in 1986 by Gerlowski LE and Matsumura Y *et al.*, EPR effect has been widely exploited in investigations of nanomaterials as anti-cancer therapies and serves as the preclinical basis for the applicability of nanodrugs [6, 7, 8]. Despite exciting preclinical results of the EPR effect,

the therapeutic efficacy of many current nanomedicines is still low, resulting in only marginal improvement of the overall survival rate [9, 10]. This is likely attributable to the complex vascular network and complex endothelial lining contained within the real human tumor environment [10, 11]. Therefore, there is a strong impetus to improve therapeutic efficacy of nanomedicines by enhancing the EPR effect in tumors. Toward this end, vasoactive factors such as ACE inhibitors, PGE1 agonists, and nitroglycerin have been employed to improve tumor vessel permeability [12]. However, systemic administration of these non-targeting agents may cause toxicity and off-target effects in normal tissues and vasculature.

In recent years, low-intensity photodynamic therapy (PDT) has emerged as a novel approach to enhance the EPR effect by increasing animal tumor vessel permeability [13, 14]. PDT is a minimally invasive, clinically approved therapeutic modality that has been used for its cytotoxic effects on various cells independent of cell types [15]. The process of PDT involves photosensitizer administration and light excitation with the corresponding wavelength to that of the photosensitizer absorption band. The activated sensitizer can then transfer the energy to nearby oxygen molecules, thereby generating cytotoxic singlet oxygen which ultimately leads to cancer cell apoptosis, robust inflammatory response, and tumor microvasculature change. The extent of vascular effects induced by PDT varies from vascular spasm to permanent vessel occlusion depending on different light fluence rate. Synder *et al.* first reported that low fluence rate HPPH-PDT could increase tumor vessel permeability and subsequently enhance tumor cell uptake of Doxil [13]. More recently, Zhen *et al.* used scanning electrical microscopy (SEM) to explore the mechanism of enhanced Doxil uptake after photodynamic therapy and found that an increased number of larger fenestrae were found on the endothelial walls of the irradiated tumors [14]. Luo *et al.* reported that systemic administration of HPPH liposomes with the near infrared laser irradiation resulted in enhanced liposomal doxorubicin accumulation in tumors [16]. However, two major limitations still exist in the application of conventional PDT in animal model to improve vessel permeability in deep-seated tumors for enhanced nanodrug delivery. First, the absorption band of the currently approved sensitizer is well below 700nm, whereas the visible excitation light is incapable of penetrating thick tissues to reach the photosensitizer located in deep-seated tumors. Second, formulation of some photosensitizers in physiological media is difficult due to their hydrophobicity. Limited by the lack of penetration of excitation light in conventional

PDT, previous studies using PDT to enhance drug accumulation could only be applied to shallow-seated tumors. Therefore, a modified PDT system is urgently needed to facilitate the activation of photosensitizers located in deeper tissues.

The improvement of conventional PDT has been achieved in our previous report by the successful construction of a near-infrared light-triggered UCNP platform for deep-seated tumor therapy [17,18]. However, to the best of our knowledge, the phenomenon of PDT-induced enhancement of nano-drug uptake in deep-seated tumors has not been studied motivating us to systematically study the effect of PDT on the vascular permeability of deep-seated tumors. In this study, the novel PDT system c(RGDyK)-SOC-UCNP-ZnPc (R-SUZn) was developed by modification of our previous system, which consisted of upconversion nanoparticles (UCNPs), amphiphilic chitosan, Zinc phthalocyanine (ZnPc), and targeting ligand c(RGDyK). UCNPs are capable of converting near-infrared (NIR) light to visible light and can be used to activate photosensitizers in deep tissues [19]. Amphiphilic chitosan can form core-shell nanoparticles through self-assembly and is widely used for drug delivery due to both its ability to increase the water solubility of hydrophobic agents and its low toxicity [20]. The c(RGDyK) moiety was conjugated to the surface of the nano-system for active targeting. As integrin $\alpha_v\beta_3$ is overexpressed on tumor vascular endothelial cells [21,22], the c(RGDyK) modification was predicted to impart a strong targeting ability of our nanoconstruct.

The enhanced accumulation of different nanoparticles after PDT in deep-seated tumors was demonstrated by overlaying 1cm pork tissue on the subcutaneous tumors. The light fluence rate and injection interval of nanoparticles after PDT treatment were optimized. Further, a two-step strategy involving PDT treatment and subsequent Doxil injection was proposed and validated on the deep-seated tumor model.

Materials and Methods

Materials

RE₂O₃ (RE = Y, Yb, and Er) was purchased from Aladdin Reagent Company. RECl₃ was prepared by dissolving the corresponding RE₂O₃ in hydrochloric acid. Following evaporation, the products were then redissolved in distilled water. Zinc (II) phthalocyanine (ZnPc, 95%, Alfa Aesar), oleic acid (OA, 90%, Aladdin), 1-octadecen (ODE, 90%, Aladdin), Hoechst 33342 (Beyotime), and 3-(4,5-dimethylthiazol-2-yl)-2,5-diphenyltetrazolium bromide (MTT, 98%, Aladdin) were used as received.

c(RGDyK) (GL Biochem), Doxil (Fudan-zhangjiang Bio-Pharmaceutical), PC-3 (human prostate carcinoma) and WPMY-1 (human prostatic stromal myofibroblast) cell lines were purchased from American Type Culture Collection (ATCC, USA). WPMY-1 and PC-3 cells were maintained in RPMI 1640 medium supplemented with 10% fetal bovine serum (FBS) and 1% penicillin/streptomycin.

Animals

All animal experiments were carried out in compliance with the Animal Management Rules of the Ministry of Health of the People's Republic of China and the guidelines for the Care and Use of Laboratory Animals of China Pharmaceutical University. Athymic nude mice were purchased from Charles River Laboratories (Shanghai, China). PC-3 cells (5×10^6) were subcutaneously injected into the upper left axillary fossa of nude mice.

Preparation of R-SUZn

NaYF_4 (Ratio of Y:Yb:Er = 0.78:0.2:0.02) nanoparticles and N-succinyl-N'-octyl chitosan (SOC, 5KDa) were synthesized as reported previously [18]. c(RGDyK)-SOC was prepared by covalent conjugation of c(RGDyK) to the amino groups of SOC as described previously [18,23]. Briefly, 10 mg c(RGDyK) was reacted with succinic anhydride at 40°C for 12hr to generate the cRGD-linker. The intermediate product was then activated with N-hydroxysuccinimide (NHS) and dicyclohexylcarbodiimide (DCC) at 50°C for 6hr (molar ratio of cRGD-linker:NHS:DCC = 1:1:1.5). The precipitate was removed by filtration (0.22 μm) and the NHS-c(RGDyK) was precipitated by the addition of acetone and diethyl ether (Vol/Vol ratio = 3:7). The activated c(RGDyK)-linker was reacted with 5 ml aqueous SOC (4 mg/mL) at room temperature for 24 hr. The mixture was dialyzed (MWCO 8000-14000) against phosphate buffer solution (PBS) and then centrifuged for 10 min at 8000 rpm to remove excess NHS-c(RGDyK). The prepared UCNP (0.5 mg) were dispersed by sonication ($P = 100 \text{ W}$) in c(RGDyK)-SOC aqueous solution (2 mg/mL). The resultant colloid solution was filtered through a 0.22 μm filter to remove large aggregates and different amounts of ZnPc (50-500 μM in DMSO) were added to 2 mL of RGD-SOC-UCNPs aqueous solution and stirred overnight. Free ZnPc was removed by centrifugation at 14000 rpm for 20 min. The final R-SUZn precipitate was washed three times with distilled water and resuspended by sonication in distilled water to form a homogeneous colloidal solution.

Characterization of R-SUZn

Morphology and size of the prepared nanoparticles were characterized using a JEOL JEM-2100 high-resolution transmission electron microscope (HR-TEM). Dynamic light scattering (DLS) was performed using a Brookhaven Nanoparticle Size Analyzer to measure the hydrodynamic diameter of particles. The PL spectra were measured using an F96 fluorescence spectrophotometer (Lengguang Technology Co. LTD, China) equipped with a xenon lamp and an external 980 nm laser (Scitower Photoelectricity Equipment Co. LTD, China).

The loading capacity and encapsulation efficiency of ZnPc in the c(RGDyK)-SOC-UCNPs were determined using spectrofluorometry by setting the excitation wavelength to 610nm and monitoring fluorescence emission over the range from 650 to 750 nm [24]. ZnPc concentration was performed in triplicate and calculated based on a calibration curve covering the range of 0.02-0.80 μM ZnPc in ethanol. A predetermined amount of R-SUZn was diluted in ethanol to obtain the range covered by the standard curve. ZnPc was ethanol extracted from the c(RGDyK)-SOC-UCNPs followed by centrifugation at 12000 rpm for 15 min to remove the c(RGDyK)-SOC-UCNPs precipitates. ZnPc content in the supernatant was then measured by spectrofluorometry. The extraction efficiency, which is defined as the ratio of fluorescence intensity of ZnPc extracted from the nanoconstructs to the fluorescence intensity of total ZnPc in the nanoconstructs, was approximately 97%. ZnPC content measurements were performed in triplicate for each formulation. Drug loading capacity of ZnPc was calculated as follows: loading capacity (%) = [mass of ZnPc in the c(RGDyK)-SOC-UCNPs (g)]/[mass of c(RGDyK)-SOC-UCNP-ZnPc (g)] $\times 100$. Encapsulation efficiency (%) was calculated as follows: Encapsulation efficiency = [mass of ZnPc in the c(RGDyK)-SOC-UCNPs (g)]/[mass of ZnPc (g)] $\times 100$.

In Vitro Drug Release

Kinetic analysis of ZnPc release was performed as described previously, with modifications. Briefly, 1 mL of R-SUZn (2 mg/mL) was dispersed in 50 mL PBS containing 2% SDS at 37°C with continuous stirring. At different time points, 3 mL of the solution was removed and centrifuged at 12000 rpm for 10 min. ZnPc present in the supernatant was measured by spectrofluorometry as described above, and the standard curve of ZnPc in the range of 0.02-0.40 μM was calibrated in phosphate buffer of various pH (5.7, 6.5 and 7.4) containing 2% SDS. The precipitates were resuspended in 3 mL of fresh medium and added to

the releasing sample again. The concentration of ZnPc released from the c(RGDyK)-SOC-UCNPs was calculated using the peak area of ZnPc emission (650-750 nm) in PBS.

Cellular Uptake study and Toxicity assay

UCL imaging was performed using confocal-compatible dishes at a density of 3×10^5 cells/dish. After incubation for 24 hr to allow for sufficient cell attachment, 200 μ L of R-SUZn was added to each confocal dish and incubated for an additional 6 hours. UCL imaging was performed using a confocal microscope equipped with an external 980 nm laser.

MTT assays were performed to determine the cytotoxic potential of R-SUZn. PC-3 and WPMY-1 cells were seeded in 96-well plates and incubated for 12 hr until confluence was reached. Cells were then treated with increasing concentrations of R-SUZn (0-800 μ g/mL). After 24 h incubation with R-SUZn, cell viability was determined using the MTT assay.

To evaluate acute toxicity of the prepared nanoconstructs in mice, a total of 80 healthy Kunming mice (50% each male and female) were randomly assigned to eight groups and injected intravenously with 200 μ L of R-SUZn (0, 20, 50, 80, 100, 140, 180, or 230 mg/kg, containing 0, 10.6, 26.5, 42.4, 53.0, 74.2, 95.4, or 121.9 mg/kg of comparable NaYF₄:Yb, Er UCNPs), respectively. Mice were weighed daily to account for any weight variation, and survival was recorded for 7 days. Blood samples were collected from the orbital sinus by removing the eyeball on day 7 post-injection for testing the biochemical parameters.

Tumor targeting assay

Athymic nude mice were purchased from Charles River Laboratories (Shanghai, China). PC-3 cells (5×10^6) were subcutaneously injected into the upper left axillary fossa of nude mice. When the tumors reached 0.5 cm in diameter, mice were used for NIR imaging. The NIR dye ICG (Indocyanine green) was encapsulated into the nanoconstructs to form SOC-UCNPs-ICG and c(RGDyK)-SOC-UCNPs-ICG. Mice were injected with SOC-UCNPs-ICG and c(RGDyK)-SOC-UCNPs-ICG at a dye dose of 10 mg/kg (5 μ l/g of mouse body weight) and then imaged at various time post-injection using an NIR imaging system. Tumor:normal skin ratios were obtained using the ROI function as follows: T/N ratio = (tumor signal-background signal)/[normal signal (muscle)-background signal]. Data are expressed as mean \pm SD (n = 3).

Evaluation of enhanced tumor uptake of liposome nanoparticles facilitated by PDT

To visualize the tumor accumulation of liposomal nanoparticles, liposomal-ICG and liposomal-Rhodamine were prepared as previously reported with slight modifications [25, 26]. The thin film/extrusion method was used with DPPC: Soy-PC:Chol:DSPE-PEG2000 at a molar ratio of 100:50:30:0.5. The formulation components were transferred to a 25 mL round-bottom flask and dissolved in 2 mL of chloroform/methanol (2:1) solution. The solvent was then rotovaporated at 37°C to form a thin film and the residual solvent was removed by overnight incubation of samples under vacuum. ICG solution (25 mg/mL) was used to hydrate the film at 60°C to yield multilamellar liposome vesicles. Finally, ultrasonic treatment was used to generate uni-lamellar liposomes. Liposomal-ICG was obtained after the removal of free ICG by dialysis. The preparation of liposomal Rhodamine followed similar procedures. Bilateral tumor models were established by subcutaneous injection of approximately 1×10^6 PC-3 cells on both sides of the axillary fossa. *In vivo* experiments were performed when the tumor reached 0.5 cm in diameter. For the surface tumor models, the animals were pre-injected with 20 mg/kg R-SUZn at a ZnPc dose of 1.75 mg/kg (n=3). At 12 h post-injection, the left side tumors were exposed to the 660nm light of 34 mW/cm² for 30 min. The right-side tumors were shielded by aluminum foil and served as internal controls. Liposomal-ICG (10 mg/kg, 10 μ l/kg of mouse body weight) was injected 2 min after laser irradiation, after which animals were subjected to fluorescence imaging on a CCD. For the deep-tissue tumor models with 1cm pork tissue overlaid on both tumor sites, R-SUZn pre-treatment was performed exactly as described above. The left and right tumors were then irradiated with 980 nm light and 660 nm light respectively, and liposomal-ICG was injected followed by NIR imaging. To visualize tumor uptake under confocal laser microscopy, animals in the single tumor models (as used in the tumor targeting assay) were injected intravenously with liposomal-Rhodamine at a dye dose of 15 mg/kg after similar R-SUZn pre-treatment as for the NIR imaging study. Mice were then sacrificed and tumor tissue sections were subjected to laser confocal imaging after nuclear staining.

Enhanced tumor uptake of HSA and gold nanoparticles

Gold nanoparticles were prepared in our laboratory as previously reported [27]. Briefly, trisodium citrate (25 mL, 38.8 mM) was added to a

boiling solution of HAuCl₄ (250 mL, 1 mM). The color of the solution changed from pale yellow to deep red within 2 minutes, indicating the formation of AuNPs. The mixture was then refluxed for 45 min to promote the formation of spherical AuNPs. HSA was conjugated with ICG through an amidation reaction to form HSA-ICG. The tumor uptake studies with gold nanoparticles and HSA-ICG were performed with procedures similar to those as described for liposomal-ICG, except that the tumor uptake of gold nanoparticles was visualized under dark field microscopy.

Optimization of light fluence rate of PDT

To study the influence of different light fluence rate on tumor uptake of nanoparticles, nude mice bearing PC-3 derived tumors at left axillary fossa with 1cm pork tissue overlaid onto tumor sites were randomly divided into 1 control group and 5 experimental groups. There were 3 mice in each experimental group. Experimental groups were injected with 20 mg/kg R-SUZn loaded with 1.75 mg/kg ZnPc followed by NIR light irradiation at different light fluence rate (10, 22, 34, 49 or 65 mW/cm²). The control group was treated with NIR light irradiation only. Subsequently, the mice received liposomal-ICG (10 mg/kg) and then were subjected to NIR imaging. The tumor/skin ratios were calculated as described above. The tumor uptake of Doxil was also evaluated under different light fluence rate. Similarly, tumor-bearing mice were treated with R-SUZn and NIR irradiation followed by intravenous injection of 10 mg/kg Doxil. Tumors were sectioned and imaged under laser confocal microscopy.

Quantitation of intratumoral doxorubicin

The intratumoral concentration of doxorubicin at different light fluence rates was determined quantitatively. Tumor-bearing nude mice were injected with free doxorubicin (10 mg/kg, 10 μL/kg of mouse body weight) and Doxil (10 mg/kg, 10 μL/kg of mouse body weight) with varying fluence rates as described above and then sacrificed. Doxorubicin was extracted from tumor samples as described previously [14, 28], and doxorubicin fluorescence was measured by fluorometric analysis (λ_{ex} =479nm, λ_{em} =490-750nm). Doxorubicin concentration was determined by comparing the peak height in experimental samples to a standard curve.

Tumor therapy studies with deep-tissue PDT and Doxil

Nude mice bearing PC-3-derived tumors were randomly assigned to 1 control group and 5 experimental groups (n=5) when the tumor diameter

reached 0.5 cm. Mice in the control group were injected with PBS while the experimental groups were injected with 20 mg/kg R-SUZn containing 1.75 mg/kg ZnPc. 12 hours post-injection, different therapeutic schedules were performed on each experimental group: (1) 660 nm light irradiation (34 mW/cm², 30 min) without Doxil injection; (2) Doxil injection without light irradiation; (3) 660 nm light irradiation (34 mW/cm², 30 min) with 1 cm pork tissue on tumor site followed by Doxil injection 2 minutes after laser exposure; (4) 660 nm light irradiation (34 mW/cm², 30 min) on superficial tumor followed by Doxil injection 2 minutes after laser exposure; (5) 980 nm light irradiation (34 mW/cm², 30 min) with 1cm pork tissue overlaid onto the tumor site followed by Doxil injection 2 minutes after laser exposure. Tumor sizes and body weights were measured every other day. Tumor volumes were measured using calipers and calculated according to the following formula: size (mm³) = length (mm) × width (mm)²/2. All mice were sacrificed and the tumors were collected 14 days after treatment. Tumor inhibition ratio (%) = $(W_c - W_t) / W_c \times 100\%$, where W_c and W_t were the average tumor weight of control group and treatment group, respectively.

Statistical Analysis

The Student's t-test was used to determine significant differences ($p < 0.05$). The quantitative data were expressed as mean ± SD.

Results and Discussion

Synthesis and characterization of R-SUZn

The synthesis of NaYF₄:Yb,Er (OA-UCNPs) was performed using the previously reported solvothermal method [18,29]. The OA-UCNP surface was successfully coated with c(RGDyK) ligand by first conjugating the carboxyl group of c(RGDyK) with the amino group of the amphiphilic N-succinyl-N'-octyl chitosan (SOC) to form c(RGDyK)-SOC, followed by hydrophobic interaction between OA-UCNPs and c(RGDyK)-SOC [18,23]. Finally, the ZnPc photosensitizer was loaded into the c(RGDyK)-SOC layer to obtain c(RGDyK)-SOC-UNCPs-ZnPc(R-SUZn). The synthetic process is diagrammed in Figure 1A. TEM imaging and DLS analysis were used to determine the appearance and size distribution of R-SUZn (Figure 1B). The distinctive thin layer surrounding the surface of the dark nanoparticles provided visual evidence of successful SOC coating to UCNPs. The inner particle core was approximately 44 nm in diameter and the overall diameter of the final R-SUZn was estimated to be 52nm (Figure 1B, TEM, inset). DLS measurements indicated that the size distribution of R-SUZn was also approximately 50nm.

The entrapment of ZnPC in our system was confirmed by the blue transparent characteristics of the solution (Figure 1C). The optical properties of the synthesized nanoconstruct with and without ZnPc were investigated. As shown in Figure 1D, under 980 nm irradiation, the fluorescence peaks of c(RGDyK)-SOC-UCNPs were around 540 and 660 nm which was well matched with the absorption peak of ZnPc. The fluorescence peak at 660 nm was dramatically quenched by increased ZnPc loading, which was attributable to fluorescence resonance energy transfer (FRET) from UCNPs to ZnPc. The fluorescence peak of UCNPs at 540 nm could be used for *in vitro* imaging. The optical properties further confirmed that c(RGDyK)-SOC-UCNPs and ZnPc were integrated into one system. Importantly, the high quenching efficiency provides a mechanistic basis for the UCNPs to furnish visible light to activate ZnPc for ROS production.

Next, the loading capacity and encapsulation efficiency were evaluated using fluorescence spectrophotometry [24]. The loading capacity increased linearly with ZnPc concentration from 10 $\mu\text{g}/\text{ml}$ to 275 $\mu\text{g}/\text{ml}$ and reached saturation when the (ZnPc: Nanoconstruct) ratio was 11% at a ZnPc concentration of 450 $\mu\text{g}/\text{ml}$ (Figure 2A). The ZnPc encapsulation efficiency gradually decreased concomitant with increasing ZnPc concentration (Figure 2B). At a ZnPc concentration of 275 $\mu\text{g}/\text{ml}$,

both high loading capacity (9%) and high encapsulation efficiency were obtained (greater than 80%). The release of ZnPc from the nanostructure as a function of pH was then investigated (Figure 2C). Liberation of ZnPc into aqueous solution was not obvious after 48 hr incubation in phosphate buffer solutions at pH 7.4 with less than 10% of ZnPc being released from the nanostructure, indicating the stability of the prepared nanoconstruct in the physiological pH condition. In contrast, approximately 18% of the ZnPc was released from the nanostructure at pH 5.7, indicating that ZnPc incorporation was unstable under low pH, which may be attributed to the dissolution of amphiphilic chitosan in an acidic milieu. However, even in this acidic environment, ZnPc detachment from the nanostructure remained below 20%, indicating that the SOC coating could effectively reduce ZnPc release. Since the photostability of R-SUZn is critical for effective PDT, R-SUZn photobleaching was analyzed by tracing its emission intensity during the 120 min 980nm light irradiation. It was observed that the level of both the red and green emissions remained at baseline indicating that R-SUZn was considerably resistant to photobleaching and, therefore, could be subjected to long periods of laser exposure for *in vitro* and *in vivo* applications (Figure 2D).

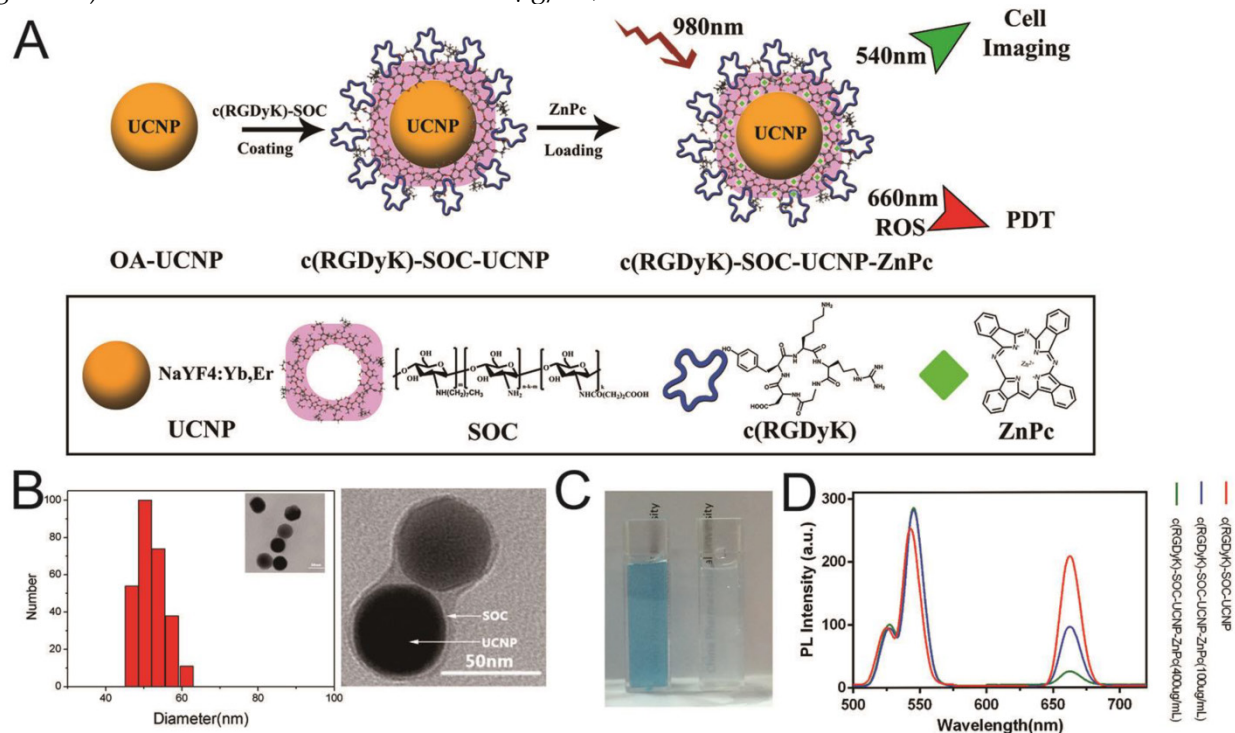


Figure 1. Synthesis and characterization of c(RGDyK)-SOC-UCNP-ZnPc (R-SuZn): (A) Experimental design of the synthetic process of c(RGDyK)-SOC-UCNP-ZnPc; (B) Morphology and size distribution of R-SuZn as demonstrated by TEM and DLS analysis; (C) Representative images of c(RGDyK)-SOC-UCNP-ZnPc (left) and c(RGDyK)-SOC-UCNP (right) under ambient light; (D) UCL emission spectra of c(RGDyK)-SOC-UCNP, c(RGDyK)-SOC-UCNP-ZnPc (100 $\mu\text{g}/\text{mL}$) and c(RGDyK)-SOC-UCNP-ZnPc (400 $\mu\text{g}/\text{mL}$).

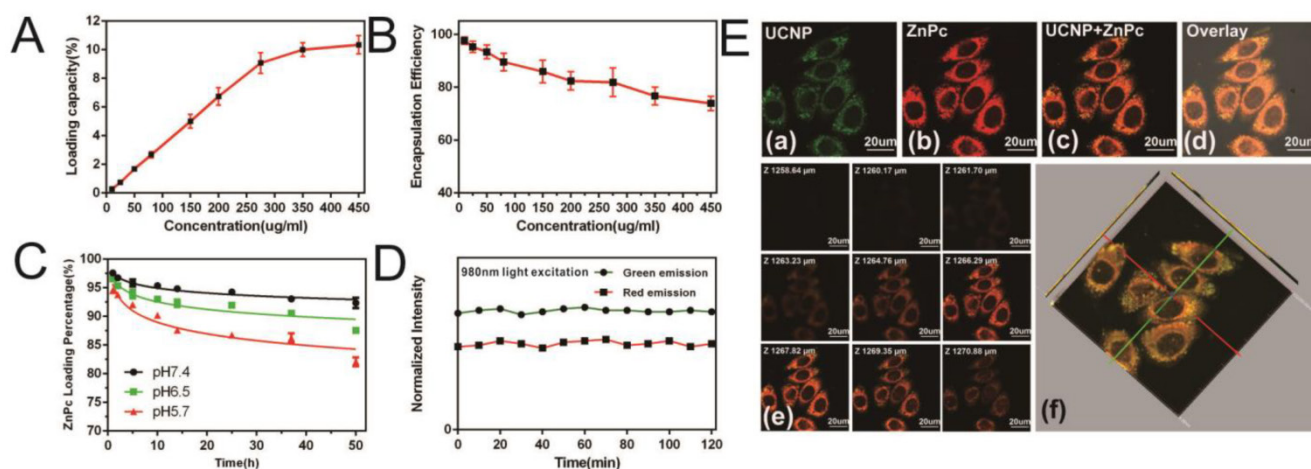


Figure 2. ZnPc loading capacity, encapsulation efficiency, and stability in PBS and *in vitro*: (A) Loading capacity at different ZnPc concentrations; (B) Encapsulation efficiencies at different ZnPc concentrations; (C) Change in ZnPc release into PBS with different pH values (5.7, 7.4 and 8.0); (D) Photostability of R-SuZn after 120min exposure to light (980nm); (E) PC-3 cells uptake of R-SuZn; colocalization of ZnPc and UCNP is indicated.

To probe the intracellular stability of the prepared nanoconstruct, R-SUZn was incubated with PC-3 cells for laser confocal microscopy imaging using 980 nm NIR laser excitation (Figure 2E). The green fluorescence of UCNP (a) and red fluorescence of ZnPc (b) were colocalized in the cytoplasm, implying that the ZnPc was stably entrapped in the nanoconstruct. Also, the results indicated that this nanoconstruct could be effectively taken up within cells for a reliable PDT efficacy. As shown in Figure 2E (e) and (f), the 2-D confocal slices and 3-D reconstruction image of PC-3 cells confirmed the exclusive colocalization of the UCNP and ZnPc in the cytoplasm without entry into the nucleus.

The results indicated that the photosensitizer ZnPc was successfully loaded into the SOC-UCNP and was minimally released from the SOC-UCNP due to both the SOC coating and the water-insolubility of ZnPc. Importantly, these imaging studies confirmed efficient cellular uptake of the ZnPc-loaded SOC-UCNP required for PDT treatment. Overall, our nanostructure showed adequate stability in physiological solutions and cellular environments, which ensures effective FRET for further *in vivo* PDT treatment.

Targeting ability and toxicity of R-SUZn

The tumor targeting ability of c(RGDyK)-conjugated nanoconstruct (R-SUZn) was evaluated in PC-3 tumor-bearing mice. Indocyanine Green (ICG) was incorporated into SOC-UCNP with or without c(RGDyK) ligand for *in vivo* imaging. As shown in Figure S1A, in the presence of c(RGDyK) ligand, the nanoconstruct showed distinct tumor accumulation at 4 hr post-injection, peaking at 12 hr and gradually decreasing afterward. In contrast, in

the absence of c(RGDyK), the tumor-localized fluorescent signal was undetectable until 8 hr after injection. The *ex vivo* experiment also showed that SOC-UCNP with c(RGDyK) ligand had higher tumor targeting effect. The ratio of tumor/normal tissue in the two groups (Figure S1B) was also determined. These results proved the favorable targeting ability of R-SUZn to $\alpha_v\beta_3$ overexpressed PC-3 tumors.

The *in vitro* toxicity of R-SUZn in PC-3 cancer cells and WPMY-1 normal cells was evaluated. The high cell viability after exposure to increasing concentrations of R-SUZn indicated the low toxicity of the prepared nanoconstruct (Figure S2A). In the 7-day acute toxicity test on the subject mice, mortality was observed at the high concentration of 100 mg/kg, and increased at higher drug doses with an LD₅₀ of 151 mg/kg (Table S1). Biochemical parameters were also determined to assay the toxicity of our nanoconstruct (Figure S2B). No obvious change in these parameters was found at doses of 50 mg/kg and 100 mg/kg. ALT (Alanine Transaminase) and AST (Aspartate Aminotransferase) levels were elevated compared to the control group at 180 mg/kg, suggesting potential hepatotoxicity of the nanoconstruct at a high dose. No significant changes in BUN (Blood Urea Nitrogen) or CREA (Creatine) levels were observed in any of the dose groups analyzed, indicating minimal nephrotoxicity or cardiotoxicity of R-SUZn. The toxicity of the nanostructure was further evaluated by H&E staining of histological sections of several major organs. As shown in Figure S2C, no observable toxicity was observed at a dose of 80 mg/kg until 7 days after treatment; however, mild inflammation was noted in the 140 mg/kg group. These results suggested that the toxicity of R-SUZn was dose-dependent, which is informative for

determining optimal doses for downstream applications.

Enhanced accumulation of different nanoparticles in deep-seated tumors facilitated by PDT

It has been reported that PDT-based methods can enhance the EPR effect of nanoparticles by increasing tumor vessel permeability [13, 14]. However, traditional PDT treatment using 660 nm excitation light suffers from insufficient tissue penetration. We used UCNPs that transform NIR light

to visible light to excite ZnPc and subsequently enhance liposome nanoparticles uptake by deep-seated tumors *in vivo*.

To investigate the improved intratumoral accumulation of the liposome particles in deep-seated tumors by UCNPs-based PDT, mice bearing PC-3-derived tumors at both axillary sites were firstly injected intravenously with R-SUZn (20 mg/kg). At 12 hr post-injection, tumors at the left axillary sites were exposed to 660 nm light of 34 mW/cm², with the non-irradiated contralateral tumors serving as internal controls. Mice were then injected with the liposomal-ICG 2 minutes after

laser exposure and subjected to fluorescent imaging to compare the accumulation in tumors at both axillary sites. As shown in Figure 3A-a, the irradiated (left side) tumors exhibited detectable fluorescence by 4 hr post injection. The intratumoral fluorescence signal peaked at 8 hr and was still detectable at 24 hr, while the fluorescence of un-irradiated (right side) tumors exhibited a much lower intensity. These phenomena verified the enhanced uptake of liposomal nanoparticles by the subcutaneous tumor after shallow tissue PDT. The improved nanoparticle uptake after PDT treatment was due to the enhanced EPR effects, which may result from the porosity of endothelial walls by PDT.

To confirm the PDT effect of our novel R-SUZn system on deep-seated tumors, 980nm NIR irradiation was used to activate R-SUZn in the deep-seated tumor model underneath the 1cm pork tissue. As shown in Figure 3A-b, distinctly different fluorescence between the left (980nm irradiation) and the right tumors (660nm irradiation) was observed over a 24 h period. The fluorescent signal emanating from tumors on the left side was significantly stronger than that on the right side at each time point. Even when the subcutaneous tumor was overlaid with pork tissue,

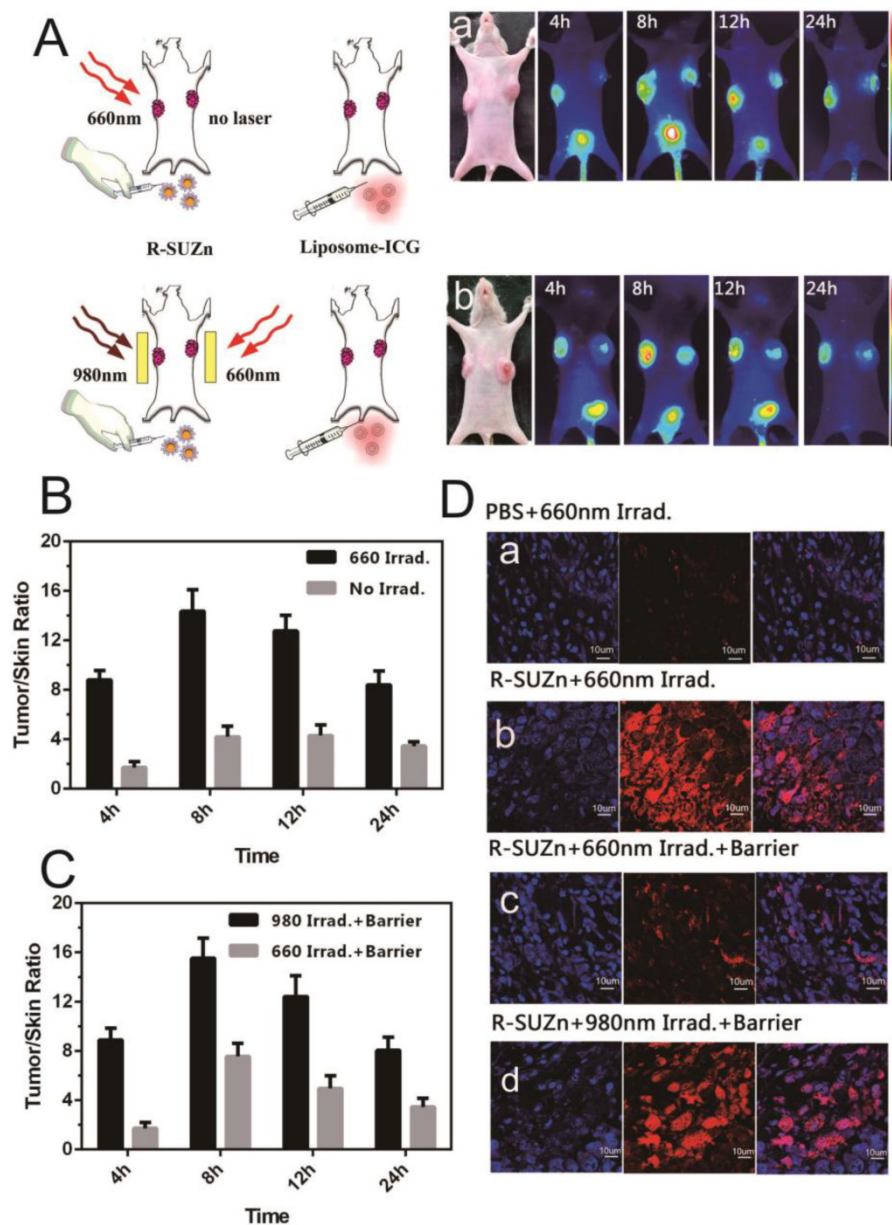


Figure 3. Enhanced tumor uptake of liposome-ICG and liposomal-Rhodamine facilitated by PDT: (A) Experimental strategy to evaluate enhanced tumor uptake of liposome-ICG in bilateral tumor models by PDT, in the absence (a) or presence (b) of a pork tissue barrier; (B) The tumor:skin ratio in superficial tumor models 24hr after 660 nm light; (C) The tumor: skin ratio in deep-seated tumor models treated with 660 nm light or 980 nm light; (D) Determination of tumor uptake of liposomal Rhodamine by laser confocal microscopy in superficial and deep-seated tumor models treated with 660nm light or 980 nm light.

using NIR light irradiation with the new PDT system, we could achieve nanoparticle accumulation comparable to that observed after traditional PDT in superficial tumor models. The tumor/skin ratios in different conditions were also plotted in Figures 3B (superficial tumor) and 3C (deep-seated tumor model), indicating that 660nm irradiation could improve the EPR effect on the superficial tumors while 980nm irradiation could enhance the EPR effect on the deep-seated tumor models. To confirm the enhanced nanoparticle uptake after various PDT treatments, the accumulations of liposomal-Rhodamine in tumor sections were imaged by laser confocal microscopy. As shown in Figure 3D-a, negligible fluorescence was observed in the control group (PBS and 660nm irradiation), possibly due to an insufficient EPR effect. Compared to control, R-SUZn combined with 660 nm laser irradiation greatly enhanced intratumoral accumulation of liposomal-Rhodamine in the superficial tumor model as indicated by markedly intensified fluorescence (Figure 3D-b). However, when pork tissue was overlaid onto the superficial tumor site, the fluorescence after 660nm light irradiation was drastically reduced (Figure 3D-c) compared to the group without the pork barrier. When NIR 980 nm light was applied in the deep-seated tumor model, significantly higher tumor fluorescence was observed,

which was comparable to that obtained using PDT with 660 nm irradiation in superficial tumor models (Figure 3D-d). These observations again demonstrated the efficacy of our new PDT platform to enhance the uptake of nanoparticles in a deep-seated tumor model and were consistent with the *in vivo* imaging results. The deep-tissue PDT effect on enhancing tumor accumulation of liposomal nanoparticles was attributed to the ability of NIR light to penetrate tissue and to the up-conversion property of UCNPs.

To further explore the impact of deep tissue PDT on intratumoral uptake of different particles, Human Serum Albumin (HSA) and gold nanoparticles instead of liposomal nanoparticles were used and their accumulation within tumors was monitored. HSA serves as a good approximation of small protein nanoparticle drugs as well as a promising drug carrier candidate, having a diameter of approximately 7nm [30, 31]. Gold nanoparticles, considered representative of metallic nanoparticles, are currently under intensive investigation as carriers of drugs, peptides and nucleotide sequences for cancer diagnosis, chemotherapy, and gene regulation [32,33]. These nanoparticles were therefore chosen to verify the versatility of this PDT platform for enhanced uptake in deep-seated tumors. After the 980nm irradiation, intratumoral HSA accumulation in the deep-seated

tumor model was obviously improved compared to the 660nm light irradiated group and was equivalent to that with 660 nm irradiation in the superficial tumor model (Figure 4A). Figure 4B shows the representative dark field images of the tumor uptake of gold nanoparticles at the tissue sections. Consistent with the above tumor uptake results, in the absence of the pork tissue barrier, tumors irradiated with 660 nm visible light showed significantly stronger fluorescence compared to control, suggesting enhanced accumulation of gold nanoparticles. Upon addition of the pork tissue, the intratumoral fluorescence after 660 nm light irradiation group markedly decreased. In comparison, larger numbers of gold nanoparticles entered tumor tissue after our novel PDT treatment. Since the enhanced intratumoral accumulation was not nanoparticle-dependent, this novel PDT system may be versatile in applications for cancer treatment using a variety of nanoparticles in deep tissues.

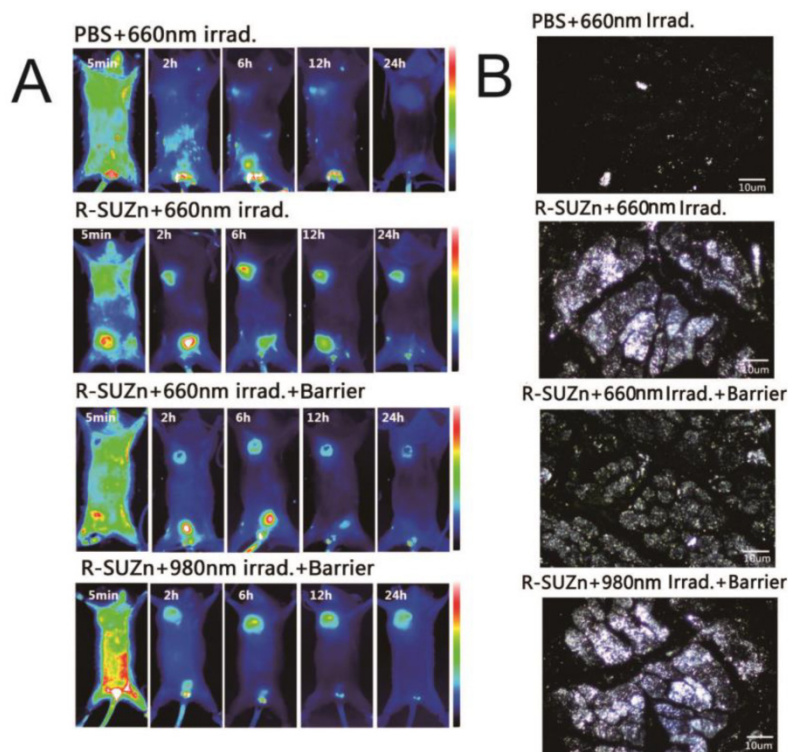


Figure 4. Enhanced tumor uptake of HSA-ICG and gold nanoparticles after PDT treatment: (A) Tumor uptake of HSA-ICG after PDT treatment in superficial and deep-seated tumor models with 660 nm or 980 nm light irradiation; (B) Dark field images of gold nanoparticles accumulation in tumor tissues after PDT treatment in superficial and deep-seated tumor models with 660 nm or 980 nm light irradiation.

Optimization of light fluence rate and injection interval of nanoparticle after PDT treatment

Previous work using conventional PDT to improve tumor uptake has demonstrated that the enhancement of EPR was dependent on light fluence rate [13]. For successful deep-tissue PDT treatment, we postulated that light fluence rate of NIR light will impact the extent of EPR effect. To test this hypothesis, subcutaneous tumors covered with 1cm pork tissues were subjected to various light fluence rate before injection of liposomal-ICG, and *in vivo* imaging was performed at various time points. As shown in Figure 5A, a weak fluorescence signal was observed in the control group with only NIR light irradiation, which may be attributed to the weak, passive targeting ability of nanoparticles. As anticipated, upon the injection of R-SUZn for PDT, the tumor-specific fluorescence initially increased concomitant with light fluence rate and reached the maximal at 34 mW/cm², followed by a declining

trend. These results confirmed our hypothesis that even in the deep-seated tumors, the extent of nanoparticle uptake varied with NIR light fluence rate, which was indeed due to different PDT effects. The optimized light fluence rate, in this case, was around 34 mW/cm². Tumor/skin ratios were also plotted in Figure 5B to quantify the fluorescence difference. As Doxil is a commonly used nanodrug in the clinic, we investigated the effect of light fluence rate on enhanced tumor uptake of Doxil. The accumulation of Doxil in tumor sites with different PDT light fluence rate was imaged by laser confocal microscopy. As shown in Figure 5C, less Doxil was observed in the control group without PDT treatment. The elevation of Doxil uptake was obvious upon the PDT treatment. Tumors in the group pretreated with PDT irradiation at 34 mW/cm² exhibited the highest fluorescence signal. The trend of light fluence rate-dependent Doxil accumulation was similar to the liposomal-ICG uptake described above.

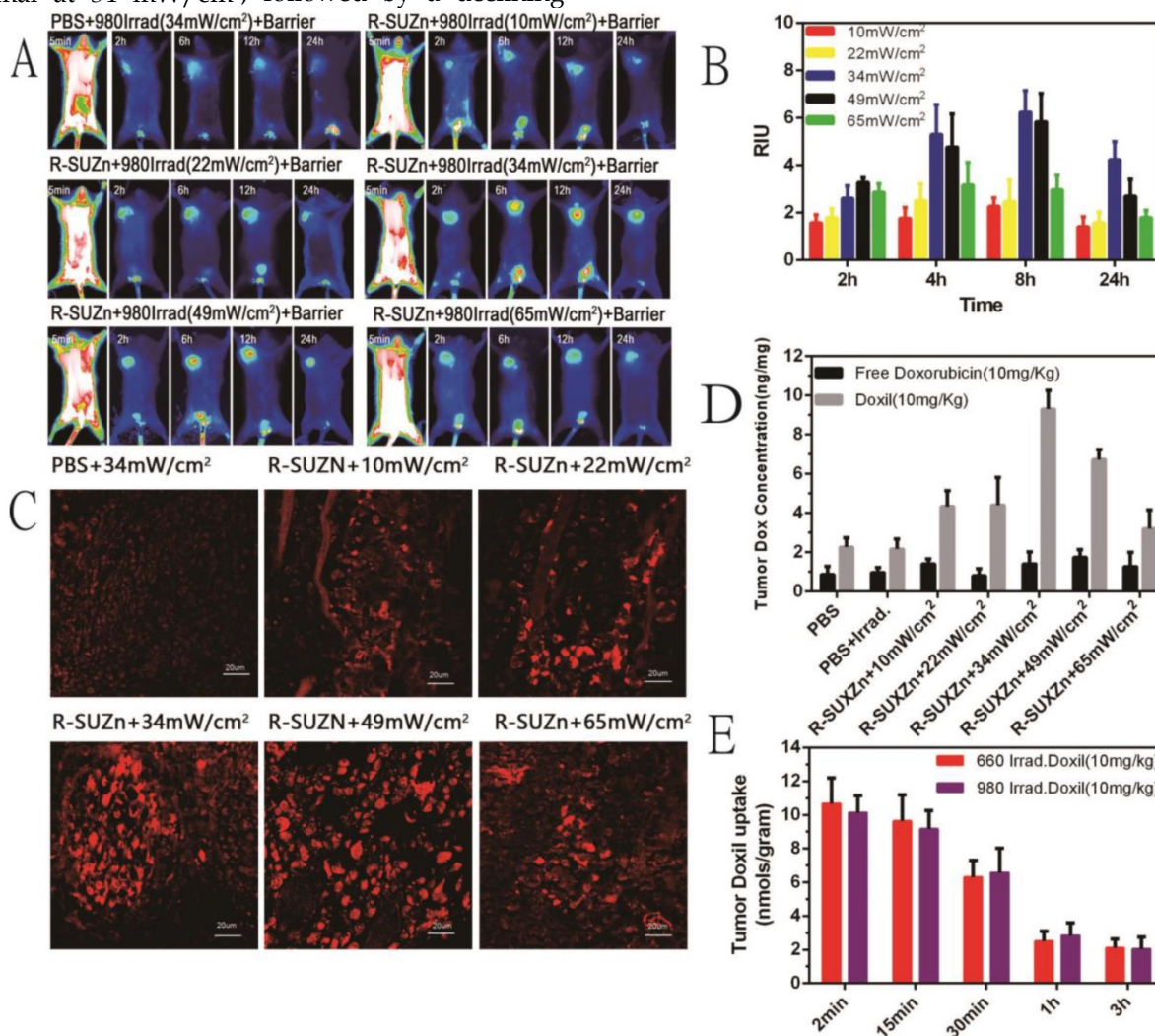


Figure 5. Effect of light fluence rate and injection interval after PDT on enhanced uptake of nanoparticles: (A) Varying tumor uptake of liposome-ICG with altered light fluence rate in deep-seated tumor models; (B) Tumor: skin ratios of liposome-ICG in mice treated with different light fluence rate; (C) Laser confocal microscopy images of tumor tissues with differing Doxil uptake under NIR light at various light fluence rate; (D) Impact of light fluence rate on intratumoral doxorubicin concentration; (E) Effect of injection interval of nanoparticle after PDT treatment on doxorubicin uptake in tumor tissues.

To illustrate the impact of PDT light fluence rate on the uptake of nanodrug and small molecule drug, mice in different groups were treated with Doxil and free doxorubicin. The mice were then sacrificed and the tumors were excised for the quantitative analysis of doxorubicin. As shown in Figure 5D, the quantity of doxorubicin extracted from tumors was significantly higher in the Doxil treated groups than in the free doxorubicin groups, demonstrating the superiority of nanodrugs for passive tumor targeting over the small molecule. Consistent with the laser confocal microscopy data, the intratumoral drug concentration increased initially with the PDT light fluence rate and decreased after the peak point. The highest accumulation of Doxil in tumor tissues was also observed at around 34 mW/cm², indicating the optimized dosage of 34 mW/cm² for the improved EPR effects. The low fluence rate may not be sufficient to alter vascular permeability while an excessively high dose could impede nanodrug penetration into tumors due to the vessel occlusion effects of PDT, which is beneficial for tumor inhibition but not for nanoparticle uptake [34]. In contrast, uptake of free doxorubicin was not affected by PDT, indicating diffusion of a small molecule to tumors is independent of the EPR effect.

The tumor uptake of nanoparticles may also be affected in part by the time interval between the PDT treatment and nanoparticle injection. To explore this possibility, Doxil was injected intravenously into tumor-bearing mice at different time points after PDT treatment, with 660nm irradiation for subcutaneous tumors and 980nm irradiation for deep-seated tumors. Mice were then sacrificed and tumors were harvested for doxorubicin extraction and quantification. As shown in Figure 5E, the intratumoral accumulation of doxorubicin was high at 2 minutes after administration of Doxil and decreased slightly within the first 15 minutes. No significant difference was observed in the initial 15 minutes after PDT. However, drug uptake was significantly reduced when the length of time between PDT and Doxil injection was extended to 30 minutes and dropped sharply after 1 hour post-PDT. These observations imply that the efficacy of PDT treatment on tumor vasculature permeability is around 30 minutes, which, along with light fluence rate, is an important consideration when PDT is used to improve drug delivery.

Improved therapeutic efficacy and reduced toxicity of Doxil by two-step treatment strategy

Based on the promising qualitative and quantitative results described above, we further

explored a two-step strategy to improve the therapeutic efficacy of nanodrug Doxil in deep-seated tumors by combining pre-treated low fluence rate PDT and Doxil administration. As shown in Figures 6A and 6B, mice treated with R-SUZn+660Irrad on the subcutaneous tumor showed no obvious tumor shrinkage compared with PBS controls, indicating that the PDT effect at 34 mW/cm² was insufficient to induce tumor cell killing. When mice received R-SUZn and Doxil without laser (R-SUZn+Doxil), obvious tumor inhibition was observed compared with the control group as a result of the antitumor efficacy of Doxil. To maximize the therapeutic effect of Doxil, low fluence rate PDT treatment (34 mW/cm²) was performed before Doxil injection to improve the accumulation of Doxil in tumor sites. As anticipated, in the absence of a pork tissue barrier, 660nm laser irradiation (R-SUZn+660Irrad+Doxil) significantly enhanced the delay in tumor growth compared to the R-SUZn+Doxil and Doxil groups. However, when 1cm of pork tissue was placed on the mouse skin to simulate deep-seated tumors, irradiation with 660 nm light (R-SUZn+Barrier+660Irrad+Doxil) displayed tumor inhibition similar to that of R-SUZn+Doxil group, indicating 660nm is unable to stimulate the PDT in the deep-seated tumor. For the group treated with NIR irradiation and Doxil (R-SUZn+Barrier+980Irrad+Doxil), robust tumor shrinkage was achieved compared with the R-SUZn+Barrier+660Irrad+Doxil group, and tumor inhibition efficiency was similar to the NIR irradiation group without barrier. These results indicated that R-SUZn PDT with 660nm laser could only improve the therapeutic efficacy of Doxil in the shallow-seated tumors rather than in deep-seated tumors. This challenge was successfully solved by our new PDT platform, which took advantage of both the NIR light with the long wavelength and UCNPs to convert NIR light into visible light. The new PDT platform (R-SUZn +980nm Irrad) could improve the accumulation of Doxil in the deep-seated tumors and thus enhance the tumor inhibition. Tumors were excised and weighed at the end of the treatment and the inhibition ratio was also calculated. As shown in Supplementary Table S2, the tumor weights and inhibition ratios were consistent with the tumor volume data (Figure 6B). In the deep-seated tumor model, enhancement of Doxil therapeutic efficacy by NIR light was comparable to that of 660nm irradiated PDT for shallow-seated tumors, with inhibition rates of 79% and 80%, respectively. Additionally, no significant change in body weight was observed across treatment groups (Figure 6C), indicating that the treatments were not detrimental to the living quality of the mice.

Histological analysis of tumor slices performed at day 14 post-treatment (Figure 6D) revealed no evidence of tumor cell death in the PBS control and R-SUZn+660Irrad groups. In contrast, Doxil treatment induced pronounced tumor cell apoptosis and necrosis. The most potent tumor apoptosis and necrosis were observed when Doxil was combined with effective PDT treatment (660 nm light on the superficial tumor or NIR light on the deep-seated tumor).

Doxorubicin is known to induce cardiotoxicity and the degree of cardiac damage increases with drug dose [35]. Given that PDT enhanced tumor accumulation of Doxil, it was hypothesized that the adverse effects of doxorubicin might be reduced by combining Doxil administration and PDT treatment.

In the absence of effective PDT, Doxil therapy caused evident damage to cardiac cells (Figure 6D), which was greatly decreased by deep-tissue PDT pre-treatment. The amelioration of cardiotoxicity was most likely due to increased routing of doxorubicin into tumor tissues, resulting in less accumulation in the heart.

In summary, we have validated that the two-step strategy, involving low fluence rate PDT treatment and subsequent Doxil injection, substantially enhances the therapeutic efficacy by improving the EPR effect of Doxil. Most importantly, doxorubicin toxicity was substantially reduced in our combinatorial therapy, providing a new avenue to improve the efficiency of conventional chemotherapy, particularly for nanoparticle-based drugs.

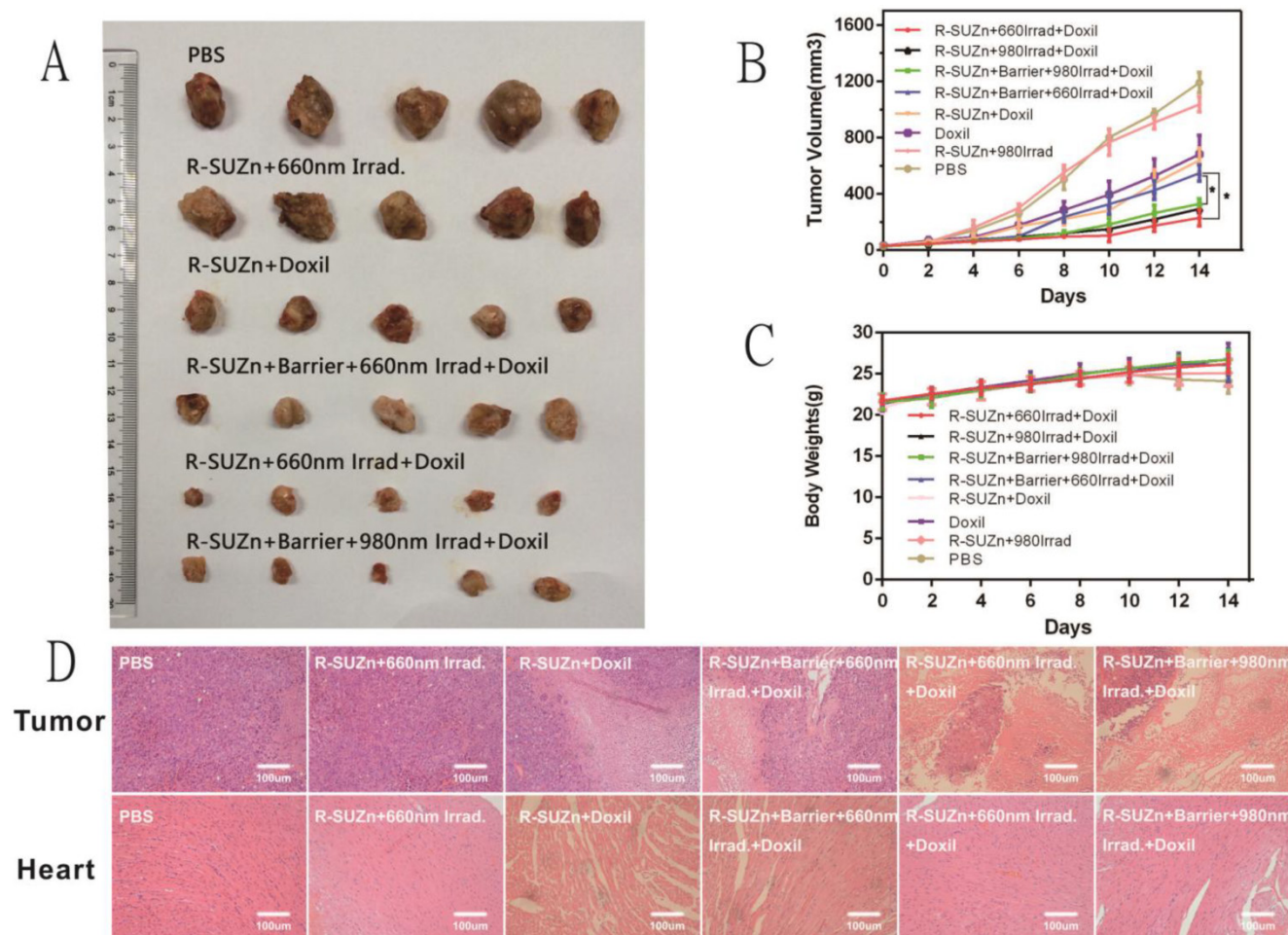


Figure 6. Therapeutic efficacy of the two-step strategy following deep-tissue PDT and Doxil injection: (A) Representative images of dissected tumors across different treatment groups; (B) Tumor volume at 14 days in different treatment groups; (C) Comparison of body weights of mice across different treatment groups over the 14-day time course; (D) H&E staining of histological sections of tumor tissues and cardiac tissue after different treatments.

Conclusion

In the present study, we synthesized a novel c(RGDyK)-SOC-UCNP-ZnPc (R-SUZn) nanoconstruct with high photosensitizer loading capacity, which exhibited selective targeting of the tumor vasculature and reduced toxicity after SOC coating. Importantly, this nanoconstruct could convert NIR light into visible spectrum light for deep-tissue PDT treatment. Although the conventional PDT was reported to enhance shallow tumor vessel permeability by enhancing the EPR effect [13, 14], this phenomenon has not been investigated in deep-seated tumors. Herein, we have reported the first use of R-SUZn-induced PDT to enhance the EPR effect in deep-seated tumors as evidenced by the augmented accumulation of different nanoparticles in tumor tissues. *In vivo* imaging and confocal microscopy of tumor samples confirmed that the novel PDT system indeed enhanced uptake of different nanoparticles in deep-seated tumors compared with traditional PDT. The PDT parameters, including PDT light fluence rate and injection interval of nanoparticles following PDT, were investigated and optimized with optimal fluence rate at 34 mW/cm² and interval time at 15 minutes. A two-step strategy, with initial PDT followed by Doxil administration, was developed to simultaneously improve the therapeutic efficacy and reduce the toxicity of Doxil in tumor-bearing mice. Increased tumor inhibition and markedly reduced cardiotoxicity were achieved through this two-step therapeutic strategy. In conclusion, our research has confirmed the application of PDT for enhanced EPR effects in deep-seated tumors and provides a novel and effective strategy to enhance the therapeutic efficacy of nanocarrier-based drugs.

Supplementary Material

Supplementary tables and figures.
<http://www.thno.org/v06p1131s1.pdf>

Abbreviations

PDT: Photodynamic Therapy; UCNPs: Upconversion Nanoparticles; EPR: Enhanced Permeability and Retention; ACE: Angiotensin Converting Enzyme; PGE1: Prostaglandin E1; SEM: Scanning Electrical Microscopy; ICG: Indocyanine Green; ZnPc: Zinc Phthalocyanine; FRET: Fluorescence Resonance Energy Transfer; NIR: Near-Infrared; ROS: Reactive Oxygen Species; HSA: Human Serum Albumin; ALT: Alanine Transaminase; AST: Aspartate Aminotransferase; BUN: Blood Urea Nitrogen; CREA: Creatine; PBS: Phosphate Buffered Saline; DLS: Dynamic Light Scattering.

Acknowledgements

We acknowledge financial support from the National Natural Science Foundation of China (NSFC 61335007, 81220108012, 81371684, 81000666, 81171395 and 81328012); the 973 Key Project (2015CB755504); and the Priority Academic Program Development of Jiangsu Higher Education.

Competing Interests

The authors have declared that no conflict of interest exists.

References

- Mitragotri S, Anderson DG, Chen X, Chow EK, Ho D, Kabanov AV, et al. Accelerating the Translation of Nanomaterials in Biomedicine. *ACS nano*. 2015; 9: 6644-54.
- Jin L, Zeng X, Liu M, Deng Y, He N. Current progress in gene delivery technology based on chemical methods and nano-carriers. *Theranostics*. 2014; 4: 240-55.
- Etheridge ML, Campbell SA, Erdman AG, Haynes CL, Wolf SM, McCullough J. The big picture on nanomedicine: the state of investigational and approved nanomedicine products. *Nanomedicine: NBM*. 2013; 9: 1-14.
- Zhang F, Zhu L, Liu G, Hida N, Lu G, Eden HS, et al. Multimodality imaging of tumor response to doxil. *Theranostics*. 2011; 1: 302-9.
- Muthu MS, Leong DT, Mei L, Feng SS. Nanotheranostics - application and further development of nanomedicine strategies for advanced theranostics. *Theranostics*. 2014; 4: 660-77.
- Gerlowski LE, Jain RK. Microvascular permeability of normal and neoplastic tissues. *Microvascular research*. 1986; 31: 288-305.
- Matsumura Y, Maeda H. A new concept for macromolecular therapeutics in cancer chemotherapy: mechanism of tumoritropic accumulation of proteins and the antitumor agent smancs. *Cancer research*. 1986; 46: 6387-92.
- Kobayashi H, Watanabe R, Choyke PL. Improving conventional enhanced permeability and retention (EPR) effects; what is the appropriate target? *Theranostics*. 2013; 4: 81-9.
- Park K. Facing the truth about nanotechnology in drug delivery. *ACS nano*. 2013; 7: 7442-7.
- Maeda H, Matsumura Y. EPR effect based drug design and clinical outlook for enhanced cancer chemotherapy. *Advanced drug delivery reviews*. 2011; 63: 129-30.
- Durymanov MO, Rosenkranz AA, Sobolev AS. Current Approaches for Improving Intratumoral Accumulation and Distribution of Nanomedicines. *Theranostics*. 2015; 5: 1007-20.
- Maeda H, Nakamura H, Fang J. The EPR effect for macromolecular drug delivery to solid tumors: Improvement of tumor uptake, lowering of systemic toxicity, and distinct tumor imaging in vivo. *Advanced drug delivery reviews*. 2013; 65: 71-9.
- Snyder JW, Greco WR, Bellnier DA, Vaughan L, Henderson BW. Photodynamic therapy: a means to enhanced drug delivery to tumors. *Cancer research*. 2003; 63: 8126-31.
- Zhen Z, Tang W, Chuang YJ, Todd T, Zhang W, Lin X, et al. Tumor vasculature targeted photodynamic therapy for enhanced delivery of nanoparticles. *ACS nano*. 2014; 8: 6004-13.
- Agostinis P, Berg K, Cengel KA, Foster TH, Girotti AW, Gollnick SO, et al. Photodynamic therapy of cancer: an update. *CA: a cancer journal for clinicians*. 2011; 61: 250-81.
- Luo D, Carter KA, Razi A, Geng J, Shao S, Lin C, et al. Porphyrin-phospholipid liposomes with tunable leakiness. *Journal of controlled release : official journal of the Controlled Release Society*. 2015; 220: 484-94.
- Cui S, Yin D, Chen Y, Di Y, Chen H, Ma Y, et al. In vivo targeted deep-tissue photodynamic therapy based on near-infrared light triggered upconversion nanoconstruct. *ACS nano*. 2013; 7: 676-88.
- Cui SS, Chen HY, Zhu HY, Tian JM, Chi XM, Qian ZY, et al. Amphiphilic chitosan modified upconversion nanoparticles for in vivo photodynamic therapy induced by near-infrared light. *J Mater Chem*. 2012; 22: 4861-73.
- Wang C, Cheng L, Liu Z. Upconversion nanoparticles for photodynamic therapy and other cancer therapeutics. *Theranostics*. 2013; 3: 317-30.
- Luk BT, Fang RH, Zhang L. Lipid- and polymer-based nanostructures for cancer theranostics. *Theranostics*. 2012; 2: 1117-26.
- Zhang Y, Yang Y, Cai W. Multimodality Imaging of Integrin alpha(v)beta(3) Expression. *Theranostics*. 2011; 1: 135-48.
- Chen K, Chen X. Integrin targeted delivery of chemotherapeutics. *Theranostics*. 2011; 1: 189-200.
- Melemenidis S, Jefferson A, Ruparelia N, Akhtar AM, Xie J, Allen D, et al. Molecular magnetic resonance imaging of angiogenesis in vivo using polyvalent cyclic RGD-iron oxide microparticle conjugates. *Theranostics*. 2015; 5: 515-29.

24. Ricci-Junior E, Marchetti JM. Zinc(II) phthalocyanine loaded PLGA nanoparticles for photodynamic therapy use. *International journal of pharmaceuticals*. 2006; 310: 187-95.
25. Xing Y, Zhao J, Conti PS, Chen K. Radiolabeled nanoparticles for multimodality tumor imaging. *Theranostics*. 2014; 4: 290-306.
26. Kim BK, Seu YB, Choi JS, Park JW, Doh KO. Synthesis and validation of novel cholesterol-based fluorescent lipids designed to observe the cellular trafficking of cationic liposomes. *Bioorganic & medicinal chemistry letters*. 2015; 25: 3893-6.
27. Xue J, Shan L, Chen H, Li Y, Zhu H, Deng D, et al. Visual detection of STAT5B gene expression in living cell using the hairpin DNA modified gold nanoparticle beacon. *Biosensors & bioelectronics*. 2013; 41: 71-7.
28. Kong G, Anyambhatla G, Petros WP, Braun RD, Colvin OM, Needham D, et al. Efficacy of liposomes and hyperthermia in a human tumor xenograft model: importance of triggered drug release. *Cancer research*. 2000; 60: 6950-7.
29. Li Z, Zhang Y. An efficient and user-friendly method for the synthesis of hexagonal-phase NaYF₄:Yb, Er/Tm nanocrystals with controllable shape and upconversion fluorescence. *Nanotechnology*. 2008; 19: 345606.
30. Trynda-Lemiesz L. Paclitaxel-HSA interaction. Binding sites on HSA molecule. *Bioorganic & medicinal chemistry*. 2004; 12: 3269-75.
31. Li R, Zheng K, Hu P, Chen Z, Zhou S, Chen J, et al. A novel tumor targeting drug carrier for optical imaging and therapy. *Theranostics*. 2014; 4: 642-59.
32. Chen H, Zhang X, Dai S, Ma Y, Cui S, Achilefu S, et al. Multifunctional gold nanostar conjugates for tumor imaging and combined photothermal and chemo-therapy. *Theranostics*. 2013; 3: 633-49.
33. Hong CA, Nam YS. Functional nanostructures for effective delivery of small interfering RNA therapeutics. *Theranostics*. 2014; 4: 1211-32.
34. Bhuvanewari R, Gan YY, Soo KC, Olivo M. The effect of photodynamic therapy on tumor angiogenesis. *Cellular and molecular life sciences : CMLS*. 2009; 66: 2275-83.
35. Ichikawa Y, Ghanefar M, Bayeva M, Wu R, Khechaduri A, Naga Prasad SV, et al. Cardiotoxicity of doxorubicin is mediated through mitochondrial iron accumulation. *The Journal of clinical investigation*. 2014; 124: 617-30.